Analysis of future heatwaves in the Pearl River Delta through CMIP6-WRF dynamical downscaling

Ziping Zuo[1], Jimmy C.H. Fung[1,2], Zhenning Li[1,*], Yiyi Huang[4], Mau Fung, Wong[1], Alexis K.H. Lau[1,3]

[1] *Division of Environment and Sustainability, The Hong Kong University of Science and Technology, Clear Water Bay, Hong Kong, China*

[2] *Department of Mathematics, The Hong Kong University of Science and Technology, Clear Water Bay, Hong Kong, China*

[3] *Department of Civil and Environmental Engineering, The Hong Kong University of Science and Technology, Clear Water Bay, Hong Kong, China*

[4] *Department of Hydrology and Atmospheric Sciences, University of Arizona, Tucson, AZ, USA*

submitted to *Earth's Future*

Oct 2022

**Corresponding author & address:*

Zhenning LI, Division of Environment and Sustainability, The Hong Kong University of Science and Technology, Clear Water Bay, Hong Kong, China

Abstract

Recent worldwide heatwaves have shattered temperature records in many regions. In this study, we applied a dynamical downscaling method on the high-resolution version of the Max Planck Institute Earth System Model (MPI-ESM-1-2-HR) to obtain projections of the summer thermal environments and heatwaves in the Pearl River Delta (PRD) considering three Shared Socioeconomic Pathways (SSP1-2.6, SSP2-4.5, and SSP5-8.5) in the middle and late 21st century. Results indicated that relative to the temperatures in the 2010s, the mean increases in the summer daytime and nighttime temperatures in the 2040s will be 0.7–0.8 °C and 0.9–1.1 °C, respectively. In the 2090s, they will be 0.5–3.1 °C and 0.7–3.4 °C, respectively. SSP1-2.6 is the only scenario in which the temperatures in the 2090s are expected to be lower than those in the 2040s. Compared with those in the 2010s, hot extremes are expected to be more frequent, more intense, more extensive, and longer-lasting in the future in the SSP2-4.5 and SSP5-8.5 scenarios. In the 2010s, a heatwave occurred in the PRD lasted for 6 days on average, with a mean daily maximum temperature of 34.4 °C. In the 2040s, the heatwave duration and intensity are expected to increase by 2–3 days and 0.2–0.4 °C in all three scenarios. In the 2090s, the increase in these values will be 23 days and 36.0 °C in SSP5-8.5. Moreover, a 10-year extreme high temperature in the 2010s is expected to occur at a monthly frequency from June to September.

Keywords:

Heatwaves, Shared Socioeconomic Pathways (SSPs), Dynamical downscaling, Future climate projections, Return period

Key points:

1. Heatwaves will be more frequent, more intense, and longer lasting in 2040s and 2090s in the Pearl River Delta (PRD) region.

2. SSP1-2.6 is the only scenario with a reduction in summer temperature in the 2090s compared to the 2040s over the PRD region.

3. Extreme heat events that occurred once in 10 years in the 2010s will shorten to once a month in SSP5-8.5 in the 2090s over the PRD region.

Plain language Summary:

Recent worldwide heatwaves have shattered temperature records in many regions. The Pearl River Delta (PRD) has been experiencing record-breaking heatwaves recently. People may wonder how often such severe heatwaves may occur and whether they will expand spatially in the future PRD region. To this end, we investigated summer heatwaves in the PRD by modeling three future scenarios. Three scenarios include a sustainable scenario (SSP1-2.6, Shared Socioeconomic Pathway), an intermediate scenario (SSP2-4.5), and a worst-case scenario (SSP5-8.5). Summer temperatures in all three future scenarios will keep increasing, and summer heatwaves will become more frequent, more intense, more extensive, and longer-lasting. Except for the sustainable scenario (SSP1-2.6), the summer heat environment will worsen after the mid-21st century. In the worst-case scenario, extreme heat events that occurred once in 10 years in the 2010s will shorten to once a month in the 2090s. A better understanding of heatwave trends will benefit implementing climate mitigation methods, urban planning, and improving social infrastructure.

Introduction

Greenhouse gases (GHGs) have been warming the atmosphere, land, and ocean since Industrial Revolution, and each decade in the last 40 years has been warmer than any previous decade since 1850 (IPCC, 2021). According to the Sixth Assessment Report (AR6) of the Intergovernmental Panel on Climate Change (IPCC), the global land surface temperature in 2011–2020 was 1.6 ℃ higher than that in 1850–1900. The characteristics of extreme weather and climate events are projected to change in response to the warming mean climate. Extreme hot temperature events are expected to occur more frequently and intensely with global warming. Compared with that in 1850–1900, global terrestrial 10-year extreme heat events are expected to occur 3.1 times more frequently, with an

intensity that is 1.9 ℃ higher, if the global warming level reaches 1.5 ℃ (IPCC, 2021).

The present study is focused on heatwaves, as a type of extremely high-temperature event. Heatwaves typically refer to a prolonged period of excessively hot days, although no universal definition is available. Heatwaves are usually defined in terms of absolute or relative criteria. According to an absolute criterion, a heatwave is defined as a prolonged period with daily maximum temperatures exceeding a fixed value (e.g., 35 °C) (Wang et al., 2017). According to a relative criterion, a heatwave is a prolonged period with daily maximum temperatures exceeding a certain percentile (e.g., the 90^{th} percentile) for a long-term temperature histogram (Ding et al., 2010). The present study adopts the Hong Kong Observatory's threshold for defining a heatwave event (daily maximum temperature exceeding 33 °C for at least three days) using an absolute criterion. This definition is based on the humid and hot subtropical climate in the Pearl River Delta (PRD), which is the target area of this research. Moreover, Chan et al. (2011) highlighted that help-seeking behaviors are expected to intensify when the temperature rises to 30–32 °C. For a regional heatwave analysis, the frequency, intensity, and duration of a heatwave event can be represented by metrics such as the hot day frequency (Yang et al., 2017), heatwave frequency (Perkins & Alexander, 2013), heatwave duration (Perkins et al., 2012), heatwave temperature (Perkins, 2015), very hot day hours (Shi et al., 2019), and nighttime heatwaves (Thomas et al., 2020).

Heatwaves can adversely influence human health, the ecological environment, social infrastructure, and the overall economy. Specifically, intense heatwaves can increase human morbidity and mortality. Heat-related illnesses include heat cramps, exhaustion, and stroke. Females, the elderly, and people engaged in physical work in outdoor environments are more vulnerable to extreme heat (Ebi et al., 2021). In the summer of 2003, Europe experienced the hottest heatwave recorded since 1540, which led to the death of 70,000 people (Robine et al., 2008). Many countries in the northern hemisphere suffered severe heatwaves in 2010, including China, the European continent, North Africa, the United States, and Russia. In Russia, over 55,000 people died during the heatwave (Horton et al., 2016). In 2022, record-breaking heatwaves swept through Europe, South America, India, and China, killing more than 12,000 people. Heatwaves can also exacerbate wildfires and drought. In the hot and dry meteorological conditions induced by extreme heat, the vegetation becomes devoid of moisture and can fuel wildfires that can spread extensively and burn for considerable periods. The emergence of more frequent and intense heatwaves burdens the social infrastructure, such as healthcare, power supply, and agriculture. For example, railway tracks may buckle, and roofs may melt at high temperatures. Additionally, heatwaves can deteriorate the labor productivity and overall economy, especially in low and low-middle-income countries (Chavaillaz et al., 2019). For every trillion tons of carbon emissions, the global annual productivity loss is expected to increase by 3% and 3.6% of the total GDP in representative concentration pathway (RCP) scenarios RCP4.5 and RCP8.5, respectively (Chavaillaz

et al., 2019).

To better respond and adapt to changes in future extreme climate events, IPCC AR6 established five new illustrative future scenarios, i.e., Shared Socioeconomic Pathways (SSPs): SSP1-1.9, SSP1-2.6, SSP2-4.5, SSP3-7.0, and SSP5-8.5. Different GHG emission levels were determined based on socioeconomic assumptions, climate mitigation levels, precursors of aerosols and non-methane ozone, and air pollution controls (IPCC, 2021). The RCPs used in IPCC AR5 were replaced with these new future scenarios to provide a more comprehensive overview of different climate outcomes. In the present study, three scenarios, SSP1-2.6, SSP2-4.5, and SSP5-8.5, representing low, intermediate, and very high GHG emissions, respectively, were selected to explore future climate outcomes in the mid-term (2040–2049) and long term (2090–2099). In all emission scenarios, the global surface temperature is expected to keep increasing until at least mid-century, and global warming levels of 1.5 ℃ and 2 ℃ are expected to be exceeded by the end of this century unless the GHG levels significantly decrease. Compared with 1850–1900, the global mean surface temperature in 2081–2100 will potentially increase by 1.3–2.4 °C, 2.1–3.5 °C, and 3.3–5.7 °C in SSP1-2.6, SSP2-4.5, and SSP5-8.5, respectively.

Considerable research has been performed to project the heatwave trends on both the global and regional scales using climate models. The latest IPCC AR6 projects that heatwaves in most regions worldwide will become more frequent, more intense, and longer lasting (IPCC, 2021). However, spatial heterogeneity exists in the heatwave occurrence. By the end of this century, in business-as-usual scenarios, heatwaves as severe as the Russian heatwave in 2010 will become the norm and are projected to occur every two years in regions such as southern Europe, North America, and Indonesia. (Russo et al., 2014). Projections for China show that regions such as Yangtze River and Southern China, which suffered from heatwaves in previous climate conditions, will experience more frequent and severe heatwaves under global warming (Guo et al., 2017; Wang et al., 2017). As it was released more recently, studies using the climate output dataset from phase 6 of the Coupled Model Intercomparison Project (CMIP6) are still limited to that from CMIP phase 5 (CMIP5). Compared with CMIP5, CMIP6 provides finer-resolution climate model data and a more comprehensive set of future pathways. In terms of extreme climate events, CMIP6 can capture spatiotemporal trend patterns (with the observations as reference) more accurately than CMIP5 can (Fan et al., 2020; Chen et al., 2020). Therefore, there is a growing need to update future climate projections using CMIP6 output data. Typically, the resolution of global climate models (GCMs) ranges between 100 km and 600 km, which is too coarse for regional climate analyses. Several physical processes, such as those related to cloud microphysics, deep convections, as well as topographic drags, cannot be appropriately resolved using GCMs. Therefore, by using the dynamical downscaling method to explore regional heatwaves, we downscaled the resolution of GCM to 1 km on the PRD, which is one of the most densely urbanized and populated regions worldwide. Such urban regions are expected to suffer more from extreme heat events in

the future compared with other regions (IPCC, 2021). Moreover, we considered scenario-based future urban expansion, based on the local climate zone (LCZ) prediction in the SSPs from World Urban Database (Chen et al., 2021).

This paper comprehensively describes the daytime and nighttime heatwaves trends in the PRD region in the middle of and at the end of the century under different emission pathways. The remaining paper is structured as follows: Section 2 describes the methods used and the heatwave metrics considered. Section 3 presents the research results, and Section 4 presents the concluding remarks.

1.

Data and methodology

(a)

Dynamical downscaling method

A high-resolution version of the Max Planck Institute Earth System Model (MPI-ESM), MPI-ESM-1-2-HR, which corresponds to a 1.0° × 1.0° grid spacing and 6-hourly output frequency, was used to set the initial and lateral boundary conditions to perform dynamical downscaling over the PRD. MPI-ESM-1-2-HR was selected as it had the highest horizontal resolution among all CMIP6 GCMs. In the evaluation of the multi-models in CMIP5, MPI-ESM-MR, the antecedent version of MPI-ESM-1-2-HR, outperformed the other models in simulating the East Asian monsoon regions (Camargo, 2013). Moreover, MPI-ESM-1-2-HR can effectively reproduce the temperature signals of the 20^{th} century and has projected that the global warming level from 1850 to 2080–2100 will range from 1.5 ℃ in RCP2.6 to 4.4 ℃ in RCP8.5.

The Weather Research and Forecasting (WRF) model was used as a nested regional model, driven by MPI-ESM-1-2-HR, to generate fine-resolution regional climate information pertaining to the PRD.

Land use change projection and refinement of urban geometric parameters

To match the climate simulations in different SSP scenarios, land use change simulations were performed (Chen et al., 2021). Specifically, Chen's group used the LCZ scheme to explore the future land use change in the Greater Bay Area in different SSP scenarios. First, an LCZ map of the Greater Bay Area in 2020 with a spatial resolution of 100 m was produced. Subsequently, the Global Change Analysis Model and Future Land Use Simulation Model were used to perform the LCZ simulations. The original WRF configuration contains only one urban category with a fixed value of the albedo and roughness length despite the diversity of urban areas. Chen et al. (2021) divided urban areas into 10 types with different morphological characteristics. In the present study, we allocated

different albedo and roughness length values to these 10 types of urban grids, thereby improving the wind speed and temperature predictions (Liu, 2020).

Experimental design and model configuration

To represent the climate context in different projected scenarios and stages of the 21st century, two series of time-slice simulations were performed over 2040–2049 (the 2040s) and 2090–2099 (the 2090s) in the three SSP emission scenarios. To compare the present and future trends, baseline simulations were also performed for 2011–2019 (the 2010s) in the SSP2-4.5 scenario. The three emission scenarios, i.e., SSP1-2.6 (sustainability), SSP2-4.5 (middle of the road), and SSP5-8.5 (fossil-fueled development), represent radiative forcing values of 2.6 $\mathrm{W \cdot m^{-2}}$, 4.5 $\mathrm{W \cdot m^{-2}}$, and 8.5 $\mathrm{W \cdot m^{-2}}$ in the year 2100, respectively, based on socioeconomic assumptions. Additionally, simulations driven by the European Centre for Medium-Range Weather Forecasts Reanalysis data version 5 (ERA5) for 2011–2020 were performed for bias correction.

The WRF model version 3.9.1 was initiated on May 1 for each year of the two decades and integrated from May 1 to September 30, covering the complete warm season in southern China. The period from May 1 to May 31 was treated as the soil temperature and moisture spin-up stage, and the analysis period was from 1 June to 30 September. Vertical layers were implemented in 39 eta coordinates from the surface to the stratopause, with the planetary boundary layer corresponding to dense layers. Specifically, 20 layers were assigned from the surface to an altitude of approximately 2000 m above the terrain. The horizontal resolution of the WRF model was 27 km $\times$ 27 km in its outermost domain (WRF D01), covering East and Southeast Asia and South China Sea and extending into the tropical western Pacific. WRF D02 was nested in D01 at a resolution of 9 km $\times$ 9 km, covering southern China. WRF D03 covered Guangdong province (Figure 1). The innermost domain (WRF D04), with a resolution of 1 km $\times$ 1 km, was used to resolve the fine features over the PRD. To ensure the fidelity of large-scale mean flow from MPI-ESM-1-2-HR, six-hourly grid nudging was implemented in WRF D01 during the model integration.

The planetary boundary layer physics was reflected by the Asymmetric Convective Model version 2 (ACM2) (Pleim, 2007). The cloud microphysics was reflected by the WRF single-moment 3-class scheme (Hong et al., 2004). The Kain–Fritsch scheme was implemented in WRF D01 and D02 to parameterize the cumulus convections (Kain, 2004). The Rapid Radiative Transfer Model for General Circulation Models was the radiation transfer scheme for both longwave and shortwave processes. The WRF output was configured to have an hourly frequency to effectively archive the diurnal cycle feature over the PRD.

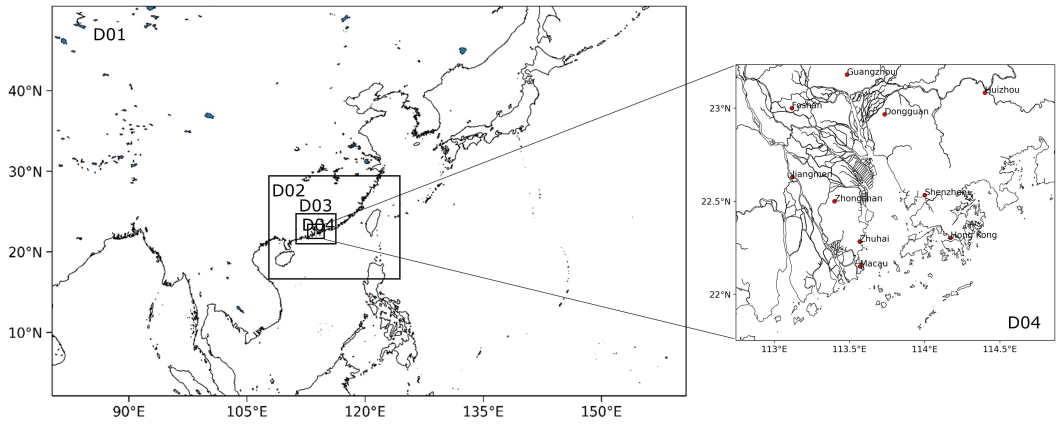

Figure 1 Horizontal coverage of WRF (Weather Research & Forecasting Model) nested domains (resolution: 27 km, 9 km, 3 km, 1 km)

Heatwave definitions

We defined a very hot day as one with the daily maximum temperature exceeding 33 ℃ and a very hot night as one with the daily minimum temperature exceeding 28 ℃ (HKO, 2022). A daytime heatwave event was defined as a period with at least three consecutive very hot days in a summer season spanning June to September. A nighttime heatwave event was considered to consist of at least three consecutive very hot nights.

We evaluated five heatwave indices (Table 1): hot day frequency (HDF), heatwave duration (HWD), heatwave temperature (HWT), hot night frequency (HNF), and nighttime heatwave duration (NHD). These indices can effectively represent the trends of magnitude, intensity, and duration of daytime and nighttime heatwaves. Moreover, the spatial plots of each index can reflect the spatial expansion of hot areas.

Table 1

Heatwave Index Definitions

Heatwave index	Definition	Unit
HDF	Mean number of very hot days each summer	Day/summer
HNF	Mean number of very hot nights each summer	Night/summer
HWD	Average duration of daytime heatwaves	Day/time
HND	Average duration of nighttime heatwaves	Night/time
HWT	Average daily maximum temperature during daytime heatwaves	℃

Return period definition

A return period is often considered in calculating the period of recurrence of extreme events such as earthquakes and floods. We applied this measure to extreme heat events. Unlike the definitions of heatwaves, we evaluated the highest hourly temperature in each grid cell from 2011 to 2020 as a 10-year extreme heat event. The highest temperature in each grid in the 2010s was used as a benchmark to calculate the return period of a 10-year extreme heat event in each scenario in future decades. The return period was calculated using Weibull's formula (Horton et al., 2016).

$$\text{return period} = \frac{n+1}{m} \# \ AUTONUM \ \ \backslash * \ GB2$$

where n is the sample size, and m is the rank of the values in decreasing order. In this study, m is the descending order rank of the highest temperatures in the 2010s, 2040s and 2090s.

Validation and bias correction of the datasets

The ERA5-driven WRF output data in hourly sequence from 2011 to 2020 (ERA5-driven) and CMIP6-driven WRF output data in hourly sequence in the SSP2-4.5 scenario (CMIP6-driven) from the same period were used to correct the systematic biases of the 2 m temperature. The bias correction was based on SSP2-4.5 owing to its pathway which is most similar to the reality of 2010s. In general, reanalysis data can reflect past weather and climate information and fill in the gaps associated with observation records and satellite data. Reanalysis data are spatially complete and consistent in time with observation records and can thus be used for bias correction. The ERA5-driven and CMIP6-driven datasets corresponded to the same WRF configuration and physics parameterization for consistency. The correction value and corrected dataset were determined using Equations (1) and (2), respectively. Figure S1 shows the spatial map of the mean correction value. CMIP6 was noted to overpredict and underpredict the 2 m temperature in inland and coastal areas, respectively.

$$\text{correction value} = \text{ERA5 driven dataset} - \text{CMIP6 driven dataset} \# \ AUTONUM \ \ \backslash * \ GB2$$

$$\text{corrected CMIP6 driven dataset} = \text{CMIP6 driven dataset} + \text{correction value} \# \ AUTONUM \ \ \backslash * \ GB2$$

The observation data of 2 m temperature in the PRD from 2016 to 2020 were used to evaluate the bias correction performance, as higher quality temperature data were available owing to the more complete data from observation stations compared with those in the other periods. All three datasets were organized in hourly frequencies to achieve the best bias correction and evaluation performance. We selected 118 observation stations for which the percentage of

missing values was less than 10%. See Figure S2 in Supporting Information for the spatial distribution of these 118 observation stations.

The following statistical metrics were calculated to evaluate the bias correction performance: mean bias (MB), mean absolute error (MAE), root mean square error (RMSE), and index of agreement (IOA), which reflect the bias and absolute error between the corrected CMIP6 dataset and observations, standard deviation of the residuals, and accuracy of the corrected CMIP6 dataset, respectively. The metrics were calculated using the following equations.

$$\mathrm{MAE} = \frac{1}{n}\sum_{1}^{n}\left(|C_m - C_o|\right) \# \ AUTONUM \ \ \backslash * \ GB2$$

$$\mathrm{MB} = \frac{1}{n}\sum_{1}^{n}\left(C_m - C_o\right) \# \ AUTONUM \ \ \backslash * \ GB2$$

$$\mathrm{RMSE} = \sqrt{\frac{1}{n}\sum_{1}^{n}\left(C_m - C_o\right)^2} \# \ AUTONUM \ \ \backslash * \ GB2$$

$$\mathrm{IOA} = 1 - \frac{\sum_{1}^{n}\left(C_m - C_o\right)^2}{\sum_{1}^{n}\left(|C_m - \overline{C_o}| + |C_o - \overline{C_o}|\right)^2} \# \ AUTONUM \ \ \backslash * \ GB2$$

where C_m is the simulation value in the grid closest to the station, C_o is the observation station value, and n is the number of observation stations.

Validation result indicates that the ERA5-driven simulation tended to overestimate the 2 m temperature by 0.6 ℃ compared with the observations. The CMIP6-driven dataset overestimated the corresponding values more than the ERA5-driven dataset. Compared with ERA5, the CMIP6-driven dataset exhibited a larger RMSE and a smaller IOA, indicating inferior performance (see Table S1 in Supporting Information). However, the bias was effectively reduced after correction, with the MB and RMSE decreasing and the IOA increasing. To precisely compare the simulations and observations, the difference associated with each observation station in the two datasets was evaluated. The CMIP6-driven simulations overpredicted the 2 m temperature at most observation stations, and this bias was effectively reduced after bias correction. The more accurate results obtained after bias correction provided a more solid basis for further analysis (see Figure S3 in Supporting Information).

1.

Results

(a)

Mean state of future thermal environment in different scenarios

i.

Decadal mean 2 m temperature in the PRD

CMIP6-driven WRF output data were used to calculate the hourly mean 2 m temperature over the 2010s, 2040s, and 2090s in different scenarios. Simulations for the 2010s in the SSP2-4.5 scenario were treated as the baseline for comparison.

Figure 2 shows the spatial pattern of the hourly mean 2 m temperature in different decades in the SSP2-4.5 scenario in the daytime (11:00 AM–4:00 PM, Local Standard Time (LST)) and nighttime (1:00 AM–6:00 AM, LST). SSP2-4.5 is the medium pathway of future GHG emissions, assuming the historical trend remains unchanged in the future. At present, the hourly mean 2 m temperature in the daytime over the land area of the PRD is 31.5 ℃. This temperature is expected to increase by 0.7 ℃ and 1.5 ℃ in the 2040s and 2090s, respectively. The nighttime hourly mean 2 m temperature in the 2010s is 26.9 ℃ and is expected to increase by 0.9 ℃ and 1.8 ℃ in the 2040s and 2090s, respectively. The rate of increase of the nighttime temperature is higher than that of the daytime temperature. The larger increase in the nighttime temperature may be caused by the increase in absorbed downward longwave radiation and anthropogenic heat. The higher rate of increase in the nighttime temperature also leads to smaller daytime and nighttime temperature amplitude in the 2040s (0.1 ℃ lower) and 2090s (0.3 ℃ lower) compared with those in the 2010s, which can increase the prevalence of heat-related diseases. The hottest locations in the PRD in both daytime and nighttime were Guangzhou and Foshan in the 2010s, but the hot area (denoted by dots) is expected to considerably expand in the future decades. The extent and intensity of this expansion will become highly severe by the 2090s, with 60% of the land area reaching a mean hourly temperature of more than 33 ℃ in the daytime and even more regions (79%) reaching a nighttime mean hourly temperature of more than 28 ℃. Compared with the 2010s, the average spatial coverage of this hot area in the 2040s is 4 and 8 times larger in the daytime and nighttime, respectively. For the 2090s, the extent is 8 and 13 times larger in the daytime and nighttime, respectively.

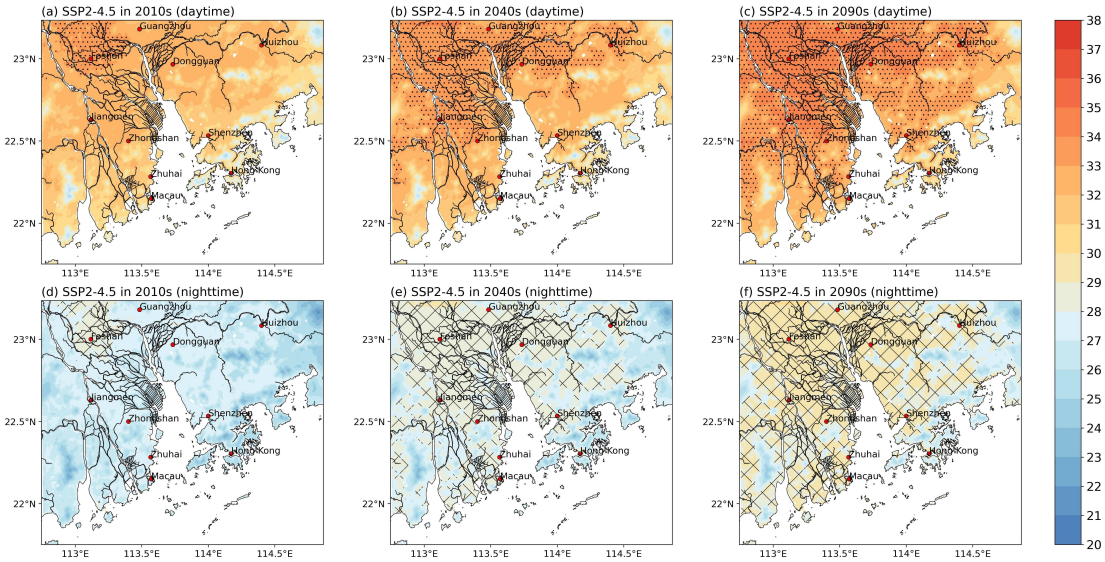

Figure 2 (a)–(c) Daytime and (d)–(f) nighttime mean 2 m temperatures in the SSP2-4.5 scenario in the 2010s, 2040s, and 2090s. Hatching areas represent areas with temperatures more than 33 °C (first row) and 28 °C (second row).

The situation in the sustainable scenario is different from those in the other two scenarios in the 2090s. Figure 3 shows the daytime and nighttime hourly mean 2 m temperature in the 2040s and 2090s in the SSP1-2.6 and SSP5-8.5 scenarios. The spatial patterns among the scenarios do not vary considerably because the CO_2 emission levels in all scenarios will continue to rise until the mid-century (IPCC, 2021). However, owing to the achievement of net zero after 2050 in SSP1-2.6, the PRD is less "hot" in the 2090s than that in the 2040s, with lower daytime (-0.3 ℃) and nighttime (-0.2 ℃) temperatures and shrunken hot areas (-10% and -7% for daytime and nighttime, respectively). Notably, the situation is pessimistic for the worst-case scenario. In the 2090s, the daytime and nighttime hourly mean 2 m temperature will increase to 34.6 ℃ and 30.3 ℃, respectively. The mean state of most locations in the PRD will even exceed the current local extreme thresholds for health cautions. In terms of the extent of hot areas, in the 2090s, 86% and 96% of land areas will reach a daytime hourly mean 2 m temperature of more than 33 ℃ and 28 ℃, respectively. Only limited areas with elevated terrain height can escape this temperature threshold.

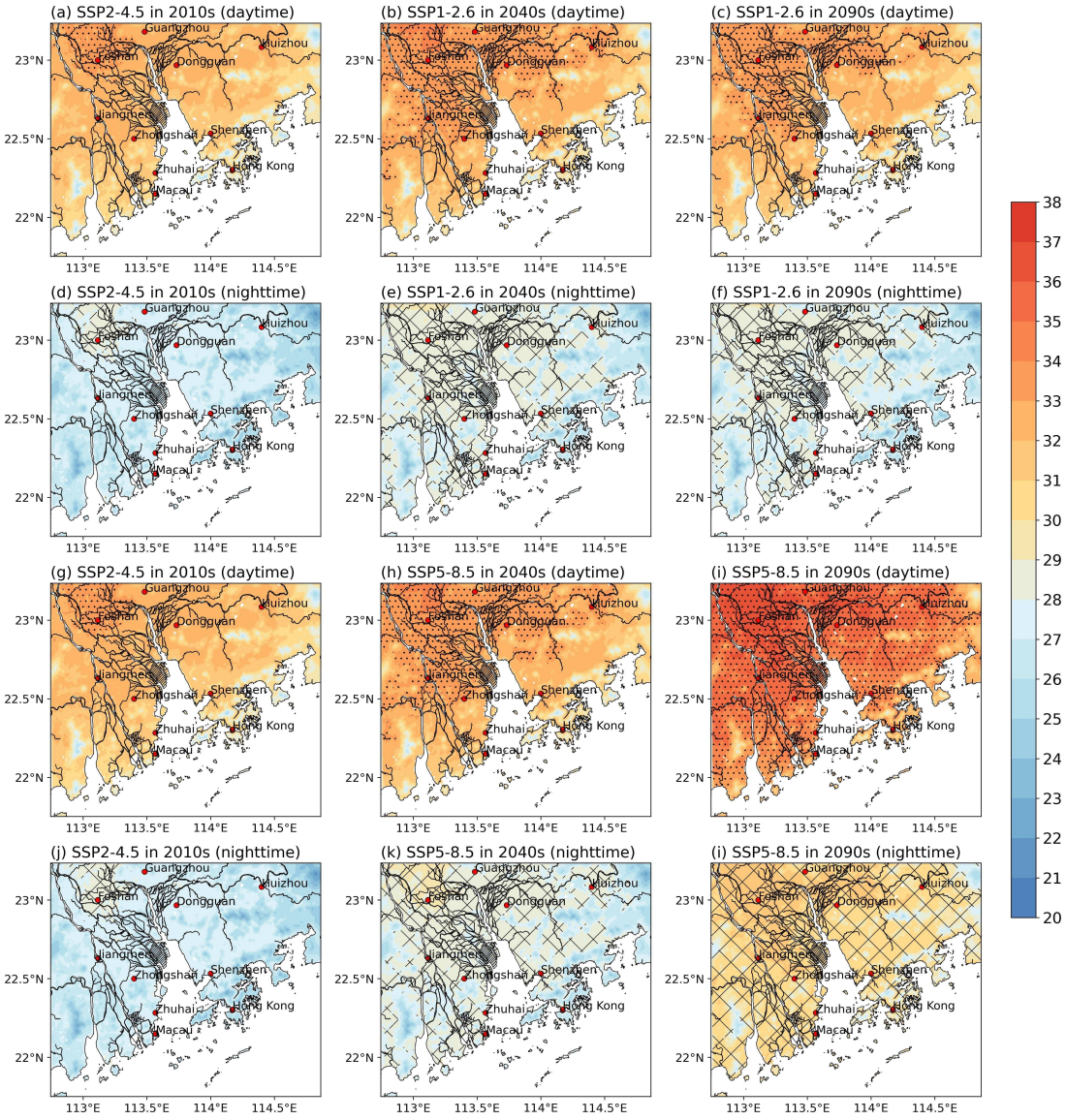

Figure 3 Mean 2 m temperatures in the 2040s and 2090s: (b), (c) Daytime and (e), (f) nighttime in the SSP1-2.6 scenario. (h), (i) Daytime and (e), (f) Nighttime in the SSP5-8.5 scenario. Hatching areas represent areas with temperatures more than 33 °C (first and third row) and 28 °C (second and fourth row).

The first column shows the values for SSP2-4.5 in the 2010s for comparison.

Probability density functions (PDFs) of 2 m temperature values

PDFs were calculated to investigate the distribution of the land hourly temperatures over different decades in different scenarios. This section focuses on the hourly 2 m temperatures over land in each scenario for each current and future period. The associated PDFs are nonparametric curves constructed through kernel density estimation and Gaussian smoothening. The vertical lines in the plots denote the statistical value of the mean of each PDF. Three statistical metrics characterizing the PDF are calculated, including the mean, variance, and skewness (Donat & Alexander, 2012). Skewness indicates the information of tails in the PDF. Positive skewness indicates that most values are clustered on the left, and the right tail is longer, with a gathering of outliers. Variance denotes how far a set of values is spread from the mean.

Figure 4 shows the PDFs of the hourly 2 m temperature (Figures 4 (a–c)), daily maximum 2 m temperature (T_{max}) (Figures 4 (d–f)), and daily minimum 2 m temperature (T_{min}) (Figures 4 (g–i)) in each scenario. In SSP2-4.5 and SSP5-8.5, the mean values of the three temperature elements increase with time; however, in SSP1-2.6, which is the emission pathway, the mean values in the 2090s shift toward slightly lower values. For SSP1-2.6, the skewness of T_{max} and T_{min} become much lower in the future decades, which means that the PDF shape deviates toward the colder part of the distribution over time. The opposite trend is observed for SSP5-8.5, with more positive skewness observed in the future. For SSP2-4.5, T_{min} becomes more positively skewed in the future, with no notable change in T_{max}. For SSP2-4.5 and SSP5-8.5, the PDFs of T_{min} and T_{max} become wider over time, as indicated by the increasing variance. In contrast, the PDFs for SSP1-2.6 become narrow over time. As indicated by the vertical line of mean values in Figure 4, the increase in the mean T_{min} is more significant than that in the mean T_{max} in SSP2-4.5 and SSP5-8.5, but this trend is not observed in SSP1-2.6 in the 2090s.

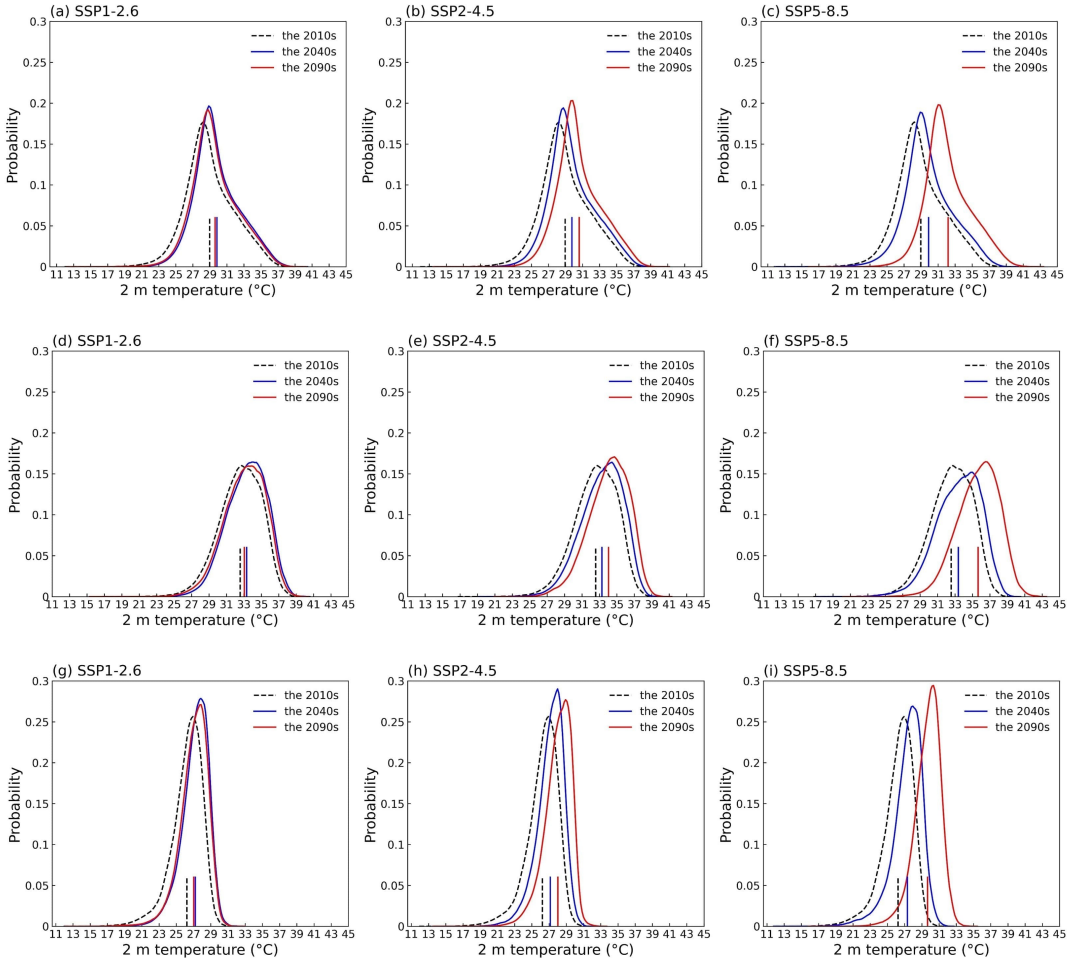

Figure 4 (a), (b), (c) Probability density function (PDF) of hourly 2 m temperature on land in the SSP1-2.6, SSP2-4.5, and SSP5-8.5 scenarios. (d), (e), (f) PDF of daily maximum 2 m temperature on land in the SSP1-2.6, SSP2-4.5, and SSP5-8.5 scenarios. (g), (h), (i) PDF of daily minimum 2 m temperature on land in the SSP1-2.6, SSP2-4.5, and SSP5-8.5 scenarios.

Figure 5 is a reconfigured version of Figure 4 to compare different scenarios in each decade. The shapes of the PDFs of different scenarios appear similar in the 2040s (similar values of the variance and skewness), and the mean values are similar as well. However, with the accumulation effect of the differences among different scenarios, which include the socioeconomic assumptions, levels of climate mitigation, and air pollution controls, significant variation is observed across different scenarios in the 2090s (IPCC, 2021).

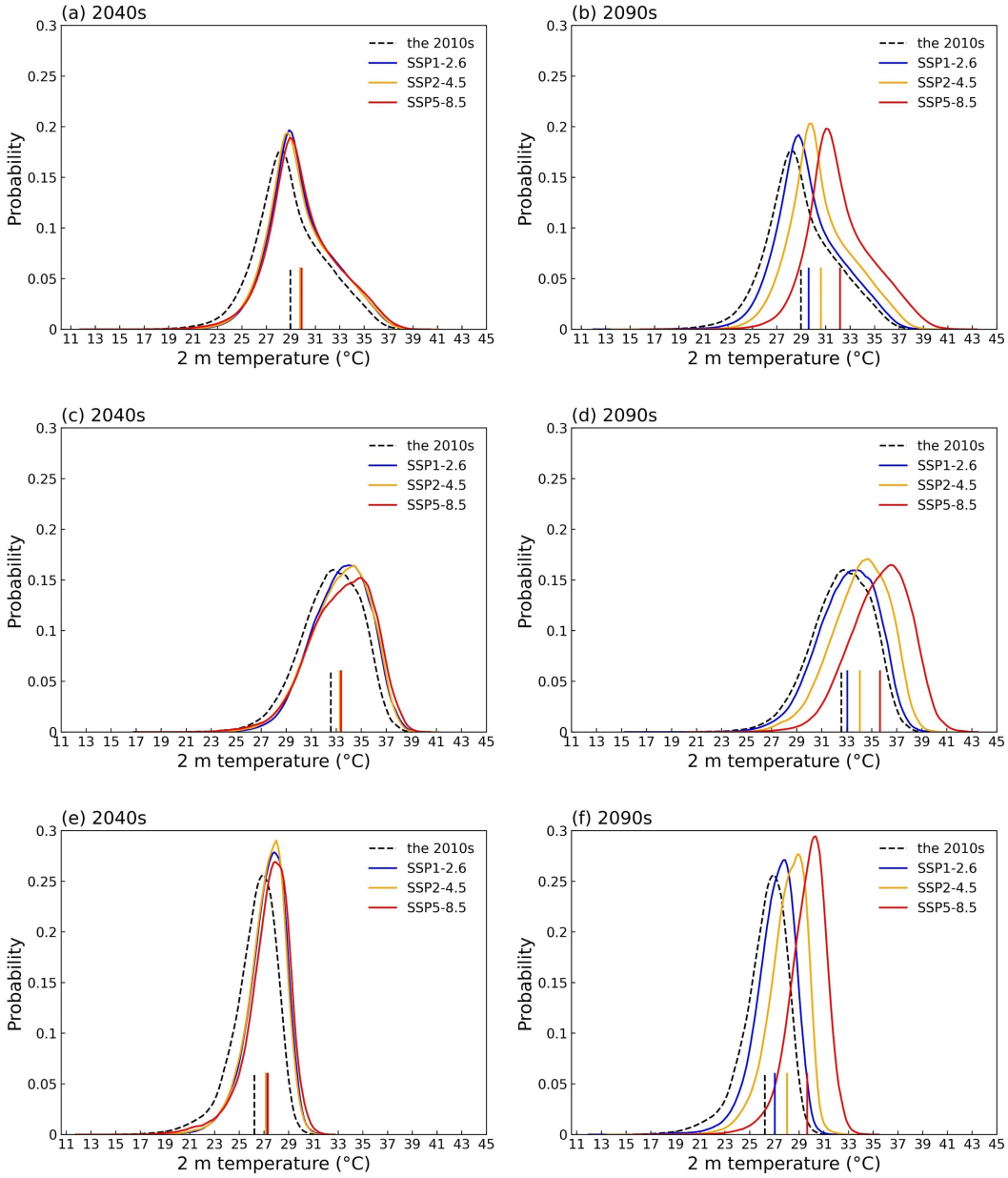

Figure 5 (a), (b) PDF of hourly 2 m temperature on land in each scenario in the 2040s and 2090s. (c), (d) PDF of daily maximum 2 m temperature on land in each scenario in the 2040s and 2090s. (e), (f) PDF of daily minimum 2 m temperature on land in each scenario in the 2040s and 2090s.

Mean state of heatwave metrics for the PRD

Heatwave metrics (HDF, HWD, and HWT) were calculated for the land area of the PRD. In the 2010s, the PRD experienced an average of 56 very hot days in the summer, and this value is expected to increase to over two months in the 2040s in different scenarios (Figure 6). In the 2090s, the difference among different scenarios will become more significant. If a more aggressive reduction scenario of GHG emission is adopted, the number of very hot days will decrease by 9%, reaching 65 in the summer of the 2090s. However, in the other two scenarios, the number of very hot days will keep increasing after the 2040s (+25% and +60% for SSP2-4.5 and SSP5-8.5, respectively).

In the 2010s, heatwave events lasted for 6 days on average. In the 2040s, the mean HWD will increase by 2 to 3 days in different scenarios, and the intensity will increase by 0.2 °C to 0.4 °C. In the 2090s, in the worst-case scenario, a heatwave event in the PRD will last for 23 days, three times longer than that in the 2010s, and the mean daily maximum temperature will reach 36 °C.

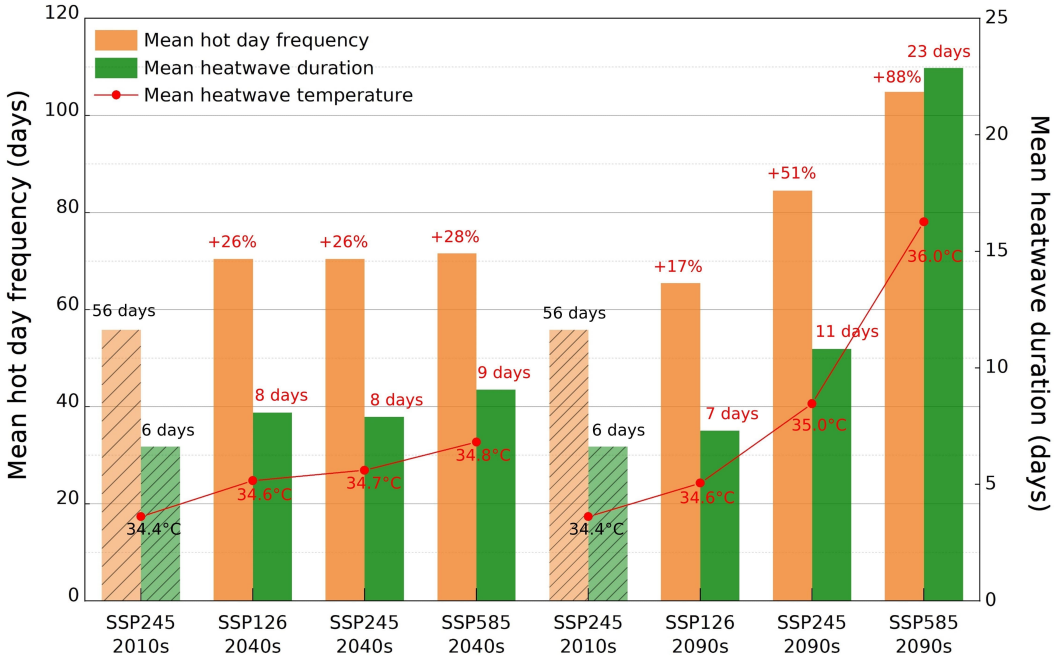

Figure 6 Hot day frequency, daytime heatwave duration, and daytime heatwave temperature spatially averaged over the land of PRD in different scenarios in different decades. The values are compared with the data for the SSP2-4.5 scenario in the 2010s.

Spatial analysis of heatwave metrics

The spatial patterns of the aforementioned heatwave metrics were plotted to clarify future extreme heat event distribution in the PRD. Sea areas are masked out from the spatial plots to highlight the land information. All the analyses in this section are based on the SSP2-4.5 scenario, an intermediate scenario in which the social, economic, and technological trends do not change significantly from historical patterns.

In the 2010s, coastal areas had fewer very hot days than inland areas, and rural areas had fewer very hot days than urban areas. For the 122 days in the experiment period, only 2,097 (9.9%) of the grid cells in the land area experienced more than 90 very hot days each summer in the 2010s. This value will increase to 8,688 (41.2%) and 13,480 (63.9%) grid cells in the 2040s and 2090s, respectively. In other words, in the 2090s, following the current trend, approximately 64% of the land area will suffer from high temperatures for over three months every summer, and 12% of the land area will have more than 110 very hot days, covering almost each summer day. Several areas of Guangzhou, Foshan, Jiangmen and Dongguan will potentially suffer most from extreme heat events in the future, as projected in the 2010s as well. Figures 7(d) and 7(e) show the differences in the HDFs between the 2040s and 2010s and those between the 2090s and 2010s. The greatest increase in the HDF corresponds to coastal areas in 2090s. This increase is not significant in the 2040s, which indicates that coastal areas will mostly become more vulnerable to such events at the end of the century.

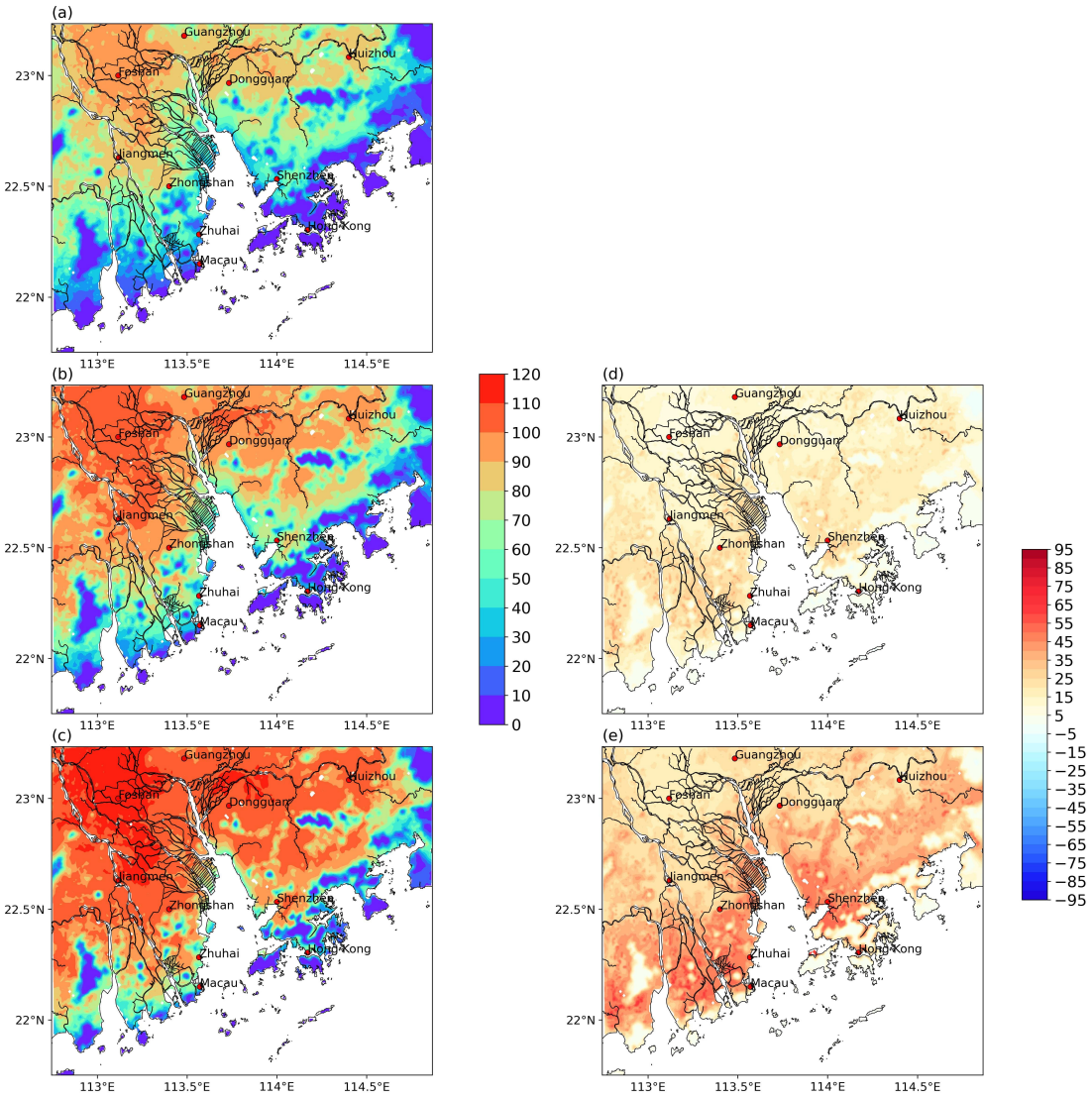

Figure 7 (a), (b), (c) Spatial plot of mean summer hot day frequency in the 2010s, 2040s, and 2090s. (d), (e) Spatial plot of the differences in the mean summer hot day frequency in the 2040s and 2010s and those in the 2090s and 2010s. All figures correspond to the SSP2-4.5 scenario.

Daytime heatwaves in Foshan last longer than in other areas in PRD in the present and will expand in the future decades. In the 2010s, on average, heatwave events lasted no more than two weeks. In the 2040s, the largest HWD will increase to 15 days (Figures 8 (a), (b)). In the 2090s, several areas in Guangzhou and Foshan may experience heat waves lasting up to 22 days (Figure 8 (c)). Despite the increase in the HDF, the HWD in several rural and coastal areas may

decrease by 1-3 days in the 2040s. However, in the 2090s, fewer areas will experience a reduction in the HWD. Foshan is expected to have the most prolonged heatwaves, along with the largest increase in the HWD (5.5 and 13.9 days in the 2040s and 2090s, respectively). For coastal areas, in the 2090s, although there is a substantial increase in individual very hot days (HDF), the largest increase in consecutive very hot days (HWD) still lies in Foshan.

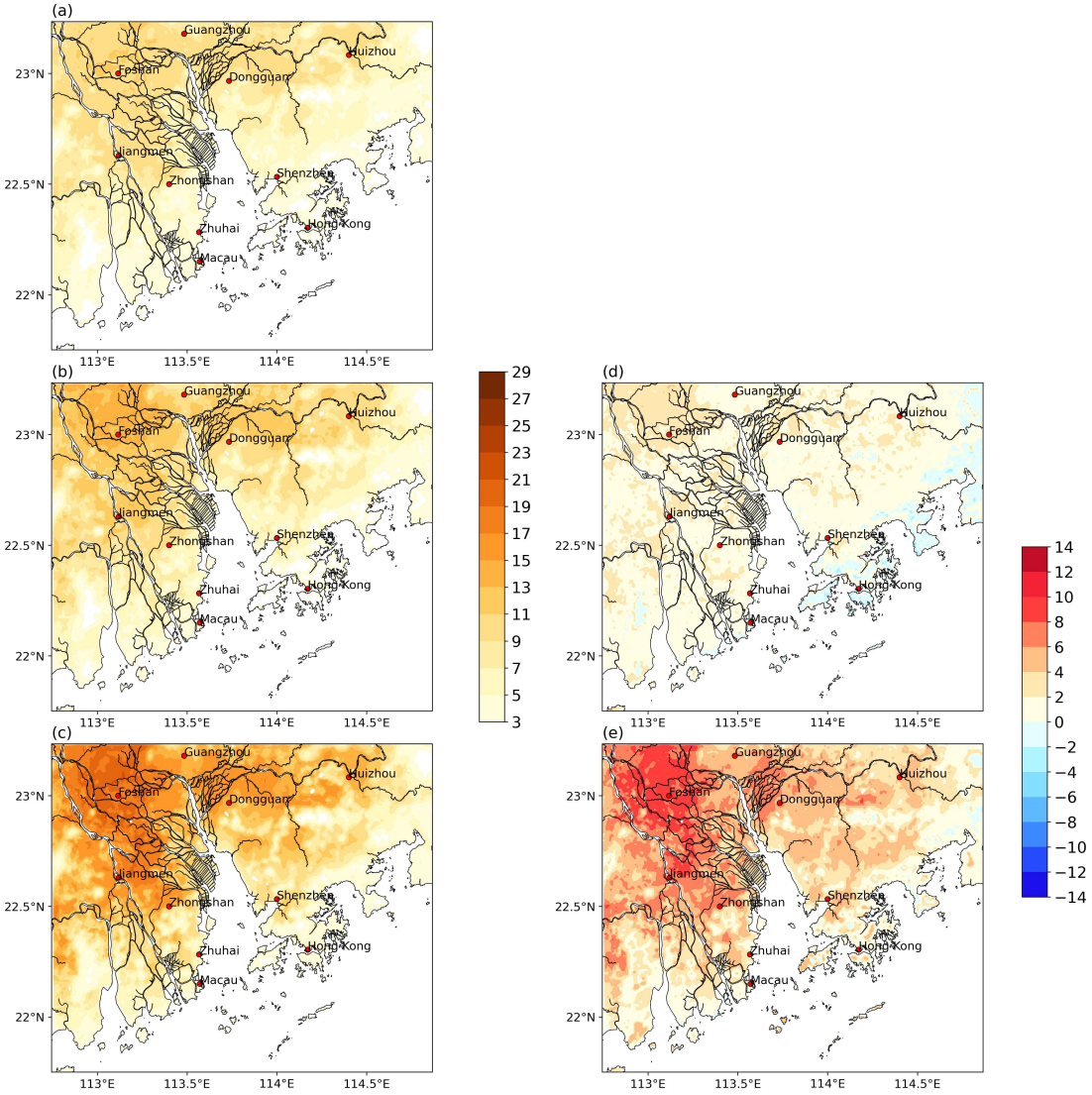

Figure 8 (a), (b), (c) Spatial plot of mean summer daytime heatwave duration in the 2010s, 2040s, and 2090s. (d), (e) Spatial plot of the differences in the mean summer daytime heatwave duration in the 2040s and 2010s and those in

the 2090s and 2010s. All figures correspond to the SSP2-4.5 scenario.

Figure 9 shows the mean temperature during a heatwave. Blank areas mean that no heatwaves occur in these locations. When a heatwave occurs in coastal areas, the daily maximum temperature ranges between 33 ℃ and 34.6 ℃, lower than that in the inland areas. In the PRD, Foshan is expected to have the most intense heatwaves, with the heatwave intensity reaching 35.9 ℃ and 36.4 ℃ in the 2040s and 2090s, respectively. Certain hotspots are observed in coastal regions caused by a single event.

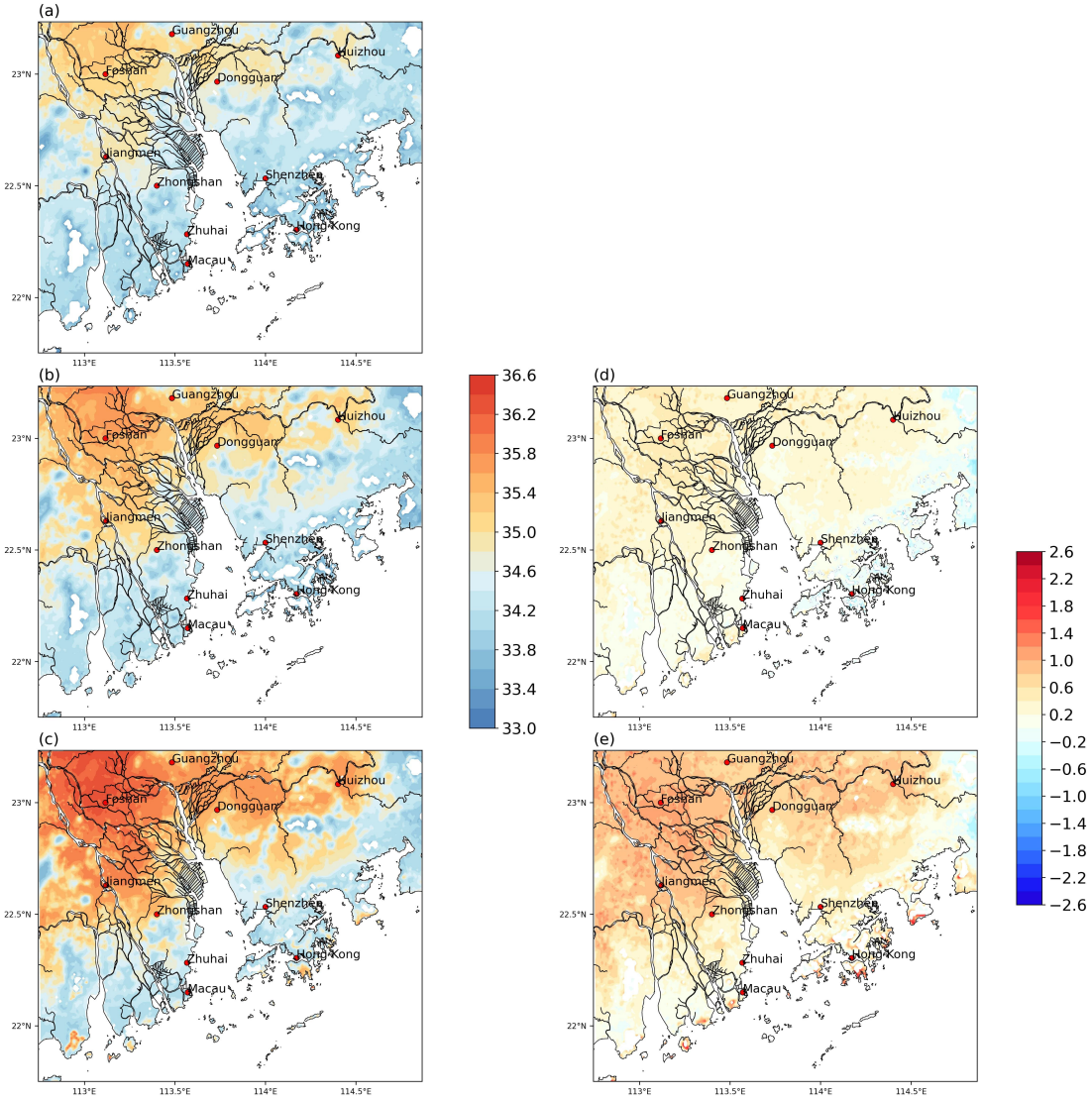

Figure 9 (a), (b), (c) Spatial plot of mean summer daytime heatwave temper-

ature in the 2010s, 2040s, and 2090s. (d), (e) Spatial plot of the differences in the mean summer daytime heatwave temperature in the 2040s and 2010s and those in the 2090s and 2010s. All figures correspond to the SSP2-4.5 scenario.

The nighttime heatwave metrics were also evaluated because consecutive hot nights may pose a more significant threat to human health than very hot days. Lower temperatures at night typically allow people to recover from the daytime heat, and the occurrence of hot nights can reduce this effect, which may lead to excess death tolls (Kovats and Hajat, 2008). Moreover, if consecutive very hot days occur with consecutive hot nights, the health impacts may be more severe than those associated with solely consecutive hot days or consecutive hot nights (Thomas et al., 2020). Among the human population, females and the elderly are more vulnerable to extremely hot weather (Wang et al., 2021). Figure 10 shows the spatial patterns of the HNF in different decades. The spatial pattern in the 2010s (Figure 10 (a)) is suggestive of the urban heat island effect, with fewer than 10 very hot nights in rural areas. With increased urbanization, more regions are expected to experience more frequent hot nights in the future. For the PRD, the spatial mean difference in the HNF is 21.7 and 50.9 nights in the 2040s and 2090s, respectively, considerably larger than the mean difference in the HDF (14.6 and 28.7 days in the 2040s and 2090s, respectively). This increase will make it challenging for people to recover from the daytime heat at night. Compared with the spatial pattern of the HDF increase, which is concentrated in coastal areas, the HNF increase is more significant and spatially dispersed, covering most of the land in the PRD.

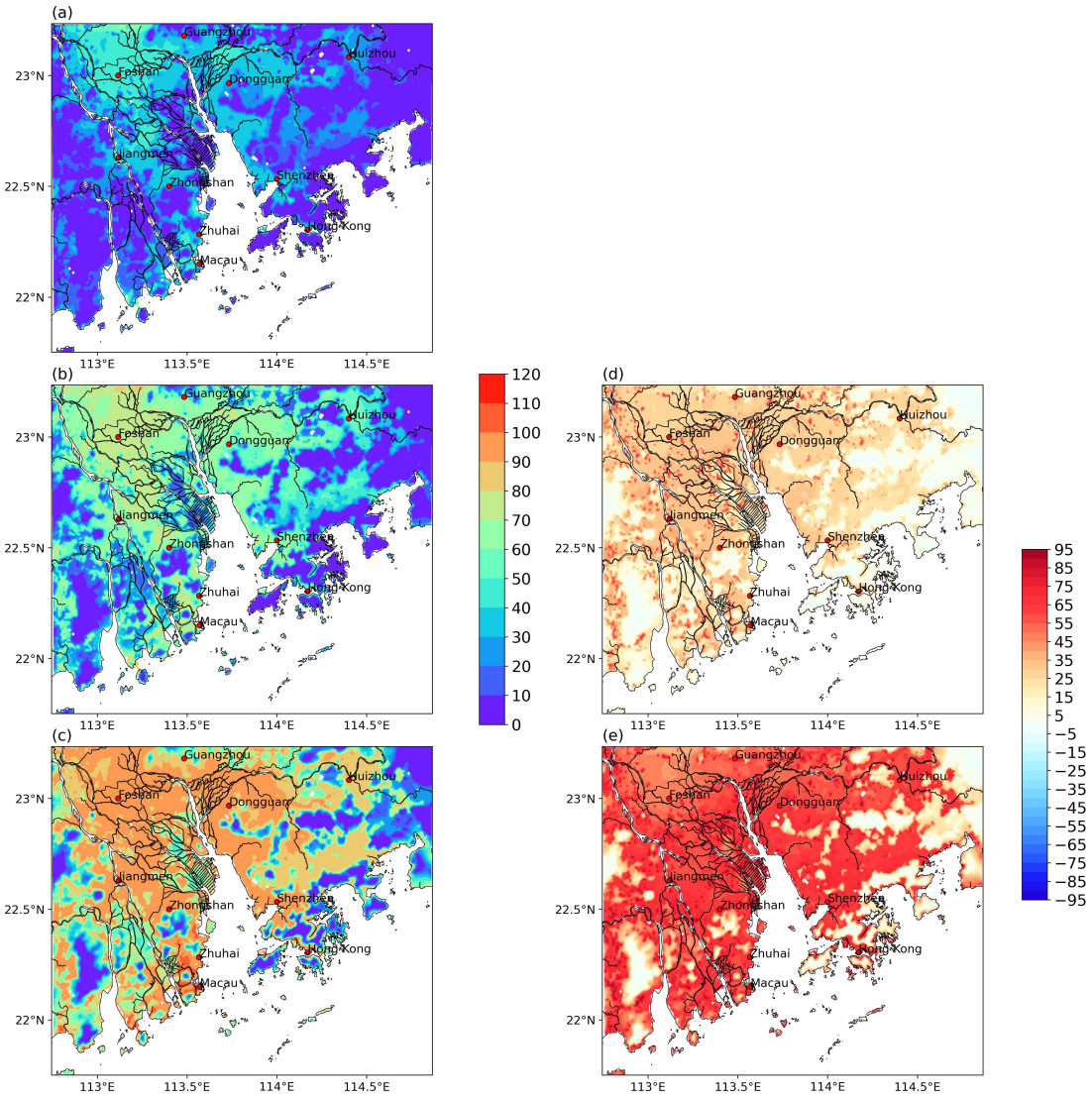

Figure 10 (a), (b), (c) Spatial plot of mean summer hot night frequency in the 2010s, 2040s, and 2090s. (d), (e) Spatial plot of the differences in the mean summer hot night frequency in the 2040s and 2010s and those in the 2090s and 2010s. All figures correspond to the SSP2-4.5 scenario.

The average NHD over the PRD in the 2010s, 2040s, and 2090s is 3.6, 5.1, and 7.7 nights, respectively. Although certain rural areas exhibit a lower NHD in the 2040s compared with that in the 2010s, the extent of these decreasing-NHD regions is smaller in the 2090s (Figures 11 (d), (e)). Better urban planning and architectural design, for instance, increased natural ventilation and green areas, can help mitigate nighttime temperatures in urban areas.

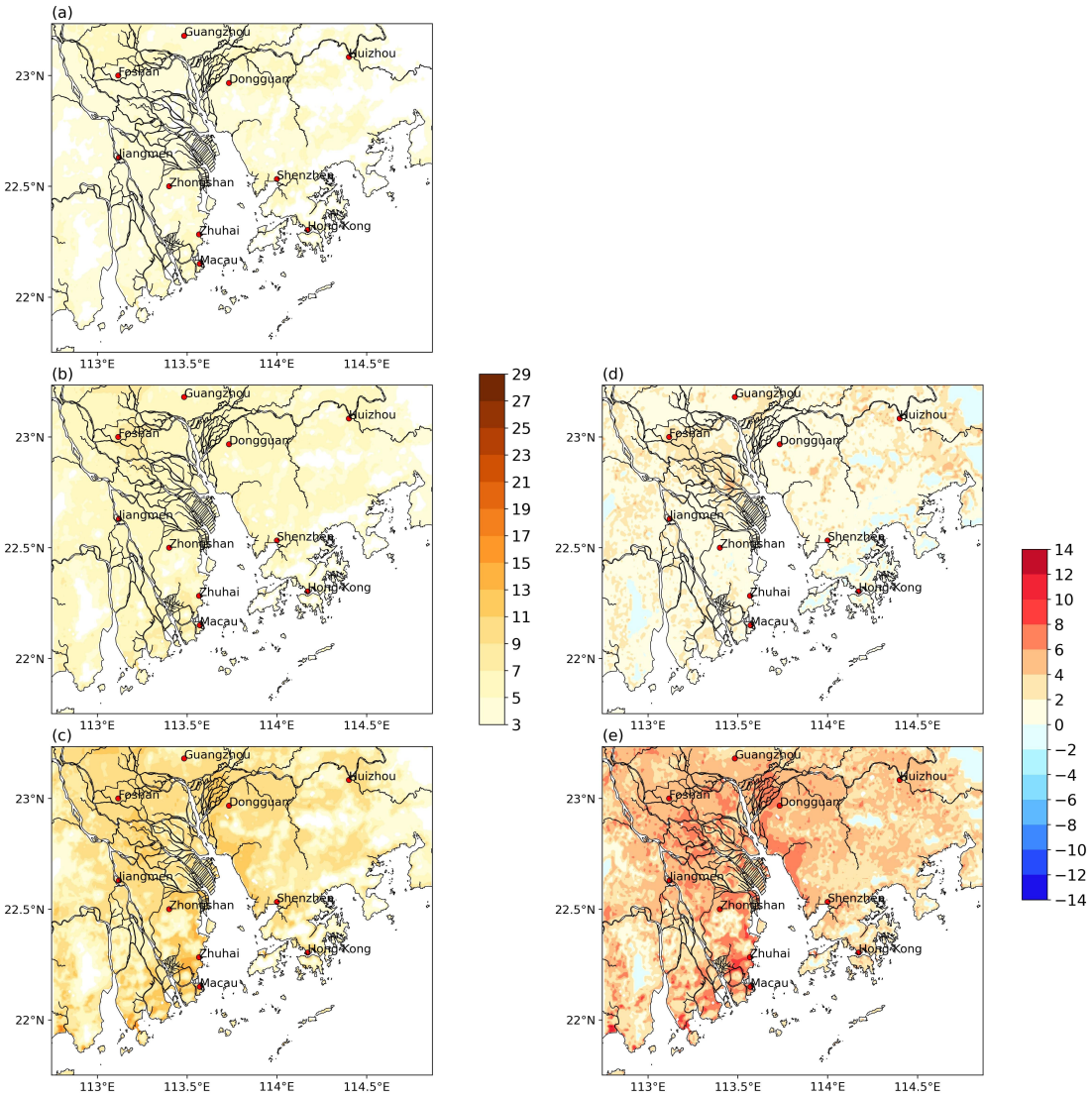

Figure 11 (a), (b), (c) Spatial plot of mean summer nighttime heatwave duration in the 2010s, 2040s, and 2090s. (d), (e) Spatial plot of the differences in the mean summer nighttime heatwave duration in the 2040s and 2010s and those in the 2090s and 2010s. All figures correspond to the SSP2-4.5 scenario.

Return period analysis

Figure 12 shows the return years in each scenario in the 2040s and 2090s relative to the once-in-a-decade event in the 2010s. The areas marked with dots and slashes correspond to return years of 0–1 and 1–2, respectively. In the

2040s, the areas with the highest extreme heat event reoccurrence are located in Guangzhou and Foshan. In the SSP1-2.6 scenario (Figures 12 (a), (b)), the range of areas with return years of 0–1 and 1-2 in the 2090s is lower than that in the 2040s. In addition, in the 2090s, Dongguan may not break the extreme temperature records corresponding to the 2010s. The spatial pattern of the return years in the SSP2-4.5 scenario is more favorable than that in SSP1-2.6 in the 2040s: the dotted and slashed areas are smaller, and more regions do not surpass the records set in the 2010s. However, in the 2090s, most locations in the PRD will suffer from the highest extreme temperature of the 2010s at least once every year or every two years. This situation is worsened in the SSP5-8.5 scenario in the 2090s, with almost every grid cell in the PRD having return year values of less than one year (Figure 11 (f)).

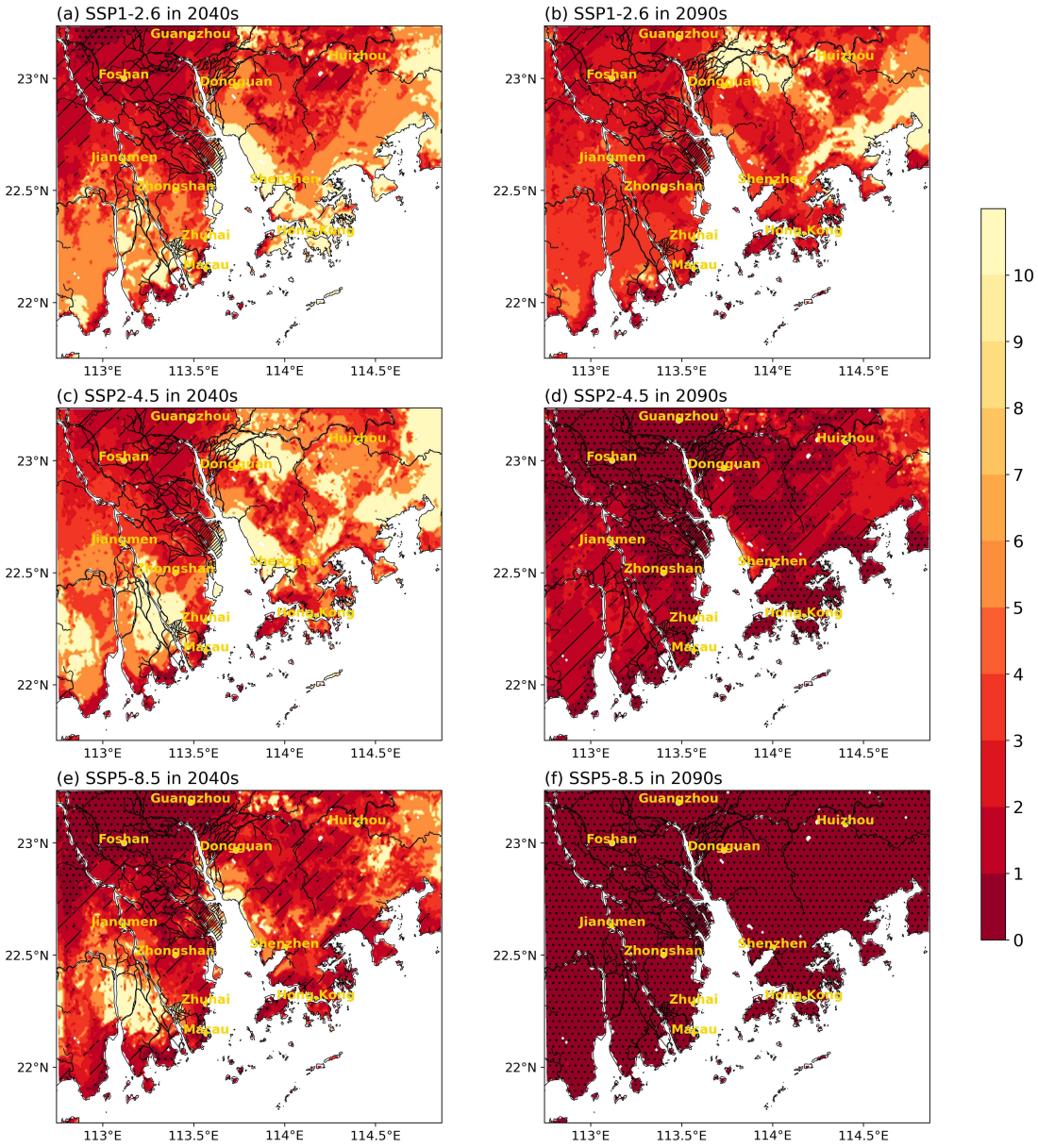

Figure 12 Return years in the 2040s and the 2090s: (a), (b) SSP1-2.6. (c), (d) SSP2-4.5. (e), (f) SSP5-8.5.

Figure 13 summarizes the increase in the frequency and intensity of extreme heat events considering the average values over the land area of the PRD. In the 2040s, an original 10-year extreme heat event will become a 4-, 4.7-, and 2.7-year event in SSP1-2.6, SSP2-4.5, and SSP5-8.5, respectively, although the

increase in intensity will be similar in all three scenarios. However, by the end of the century, the differences in both the frequency and intensity increases between the intermediate pathway (SSP2-4.5) and fossil-fueled pathway (SSP5-8.5) will become substantial. Specifically, for SSP5-8.5, the return period will decrease from 10 years in the 2010s to once in each month from June to September in the 2090s.

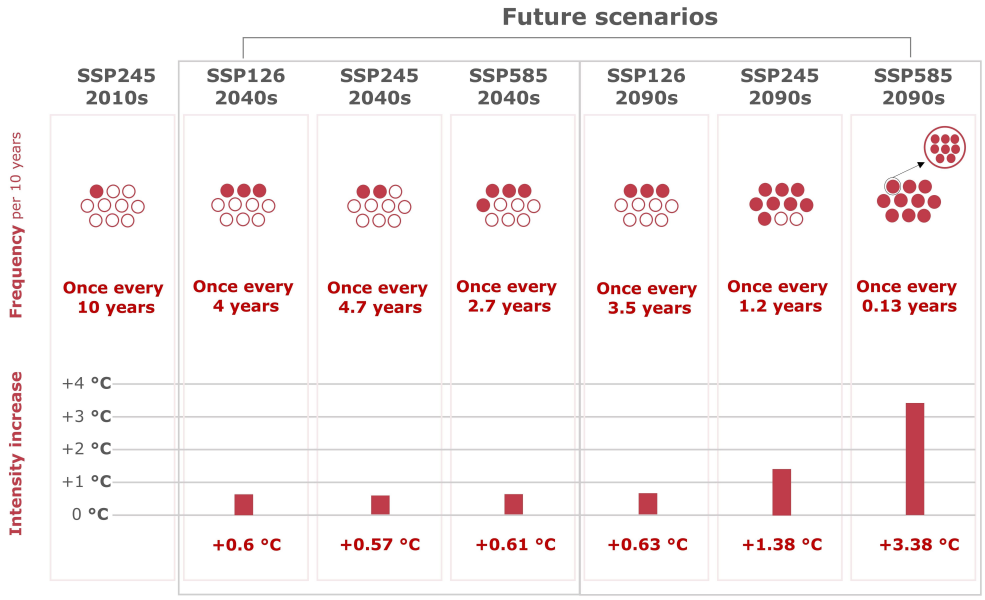

Figure 13 Increase in the frequency and intensity of hot extreme events in different scenarios in different decades.

Conclusions

A dynamical downscaling method based on the MPI-ESM-1-2-HR of CMIP6 was used to perform a comprehensive regional climate analysis. Based on the hourly 2 m temperature data over three decades (the 2010s, 2040s, and 2090s) in three future scenarios (SSP1-2.6, SSP2-4.5, and SSP5-8.5), we explored the summer thermal environment, hot extremes, and heatwaves at present and in the future. Compared with previous studies on hot extremes, our regional simulation data were driven by the newly released global climate data. Furthermore, the scenario-based projections of land use change in the mid-century were incorporated, which have rarely been considered by other research.

The results indicated that different scenarios share similar spatial patterns of the daytime and nighttime 2 m temperature in the 2040s, but the patterns significantly differ in the 2090s. SSP1-2.6, the sustainability pathway, will correspond to slightly lower daytime and nighttime temperatures in the 2090s than those in the 2040s. The opposite trends will be observed for SSP2-4.5 and SSP5-8.5,

with a significant increase in the temperature and an expansion of hot areas in the 2090s. The PDFs of the 2 m temperature were analyzed to clarify the temperature distribution in the different scenarios over time. The PDFs of the daily maximum and daily minimum temperatures will shift to higher values in SSP2-4.5 and SSP5-8.5. In contrast, the PDF of the temperature extremes in SSP1-2.6 in the 2090s will shift to lower values. The spatial patterns of different heatwave metrics suggest that parts of Guangdong, Foshan and Jiangmen will remain the hottest places in the PRD. In terms of the HDF, several coastal areas may experience more frequent hot extremes in the 2090s in SSP2-4.5. Several rural areas along the coast may suffer from a few heatwaves in which the average daily maximum temperature will exceed 35 ℃ in the 2090s. The nighttime temperature will increase faster than the daytime temperature, which may threaten human health, especially for females and individuals aged more than 70 years. According to the analysis of the spatial mean over the PRD, although the temperatures in SSP1-2.6 will decrease in the 2090s, the extreme heat frequency and intensity will not decrease considerably, and the heatwave intensity will remain the same as that in the 2040s. In the other two scenarios, the extreme heat frequency and intensity will keep increasing in the 2040s and 2090s.

Through this research, we hope to incentivize policymakers to implement appropriate mitigation measures and urban planning strategies to ensure people's comfort. Considering different future climate outcomes, different social infrastructure sectors may be equipped to better prepare for the future. Moreover, the outcomes from the worst-case scenario may serve as an alert for people to adopt more sustainable lifestyles.

This research has certain limitations. Although the urban surface characteristics were considered, the anthropogenic heat flux was not considered. Moreover, univariate definitions of heatwaves were considered, although several studies have highlighted that the combination of daytime and nighttime heatwaves may impact human health more than solely daytime and nighttime heatwaves (Wang et al., 2021).

Acknowledgement

We appreciate the assistance of the Hong Kong Observatory (HKO), which provided the meteorological data. The work described in this paper was supported by a grant from the Research Grants Council of the Hong Kong Special Administrative Region, China (Project Nos. AoE/E-603/18, C7041-21GF, R4046-18, and T31-603/21-N) and was supported by the Guangdong-Hongkong-Macau Joint Laboratory Grant GDST20IP05.

Data Availability Statement

The CMIP6 large-scale climate dataset (MPI-ESM-1-2-HR) is available at https://esgf-data.dkrz.de/search/cmip6-dkrz/. The ECMWF Reanalysis data version 5 (ERA5) used for bias correction is available at https://www.ecmwf.int/en/forecasts/datasets/reanalysis-datasets/era5. The downscaled WRF output

files, observation data, and other processed data files are preserved at Zenodo Repository https://doi.org/10.5281/zenodo.7206739. The workflow and scripts for plotting are available at Zenodo Repository https://doi.org/10.5281/zeno do.7207845 .

References

Camargo, S. J. (2013). Global and regional aspects of tropical cyclone activity in the CMIP5 models. *Journal of Climate*, *26*(24), 9880–9902. https://doi.org/10.1175/JCLI-D-12-00549.1Chavaillaz, Y., Roy, P., Partanen, A. I., Da Silva, L., Bresson, É., Mengis, N., Chaumont, D., & Matthews, H. D. (2019). Exposure to excessive heat and impacts on labour productivity linked to cumulative CO2 emissions. *Scientific Reports*, *9*(1), 1–11. https://doi.org/10.1038/s41598-019-50047-wChen, G., Xie, J., Li, W., Li, X., Hay Chung, L. C., Ren, C., & Liu, X. (2021). Future "local climate zone" spatial change simulation in Greater Bay Area under the shared socioeconomic pathways and ecological control line. *Building and Environment*, *203*(January), 108077. https://doi.org/10.1016/j.buildenv.2021.108077Ding, T., Qian, W., & Yanb, Z. (2010). Changes in hot days and heat waves in China during 1961-2007. *International Journal of Climatology*, *30*(10), 1452–1462. https://doi.org/10.1002/joc.1989Donat, M. G., & Alexander, L. V. (2012). The shifting probability distribution of global daytime and night-time temperatures. *Geophysical Research Letters*, *39*(14), 1–5. https://doi.org/10.1029/2012GL052459Ebi, K. L., Capon, A., Berry, P., Broderick, C., de Dear, R., Havenith, G., Honda, Y., Kovats, R. S., Ma, W., Malik, A., Morris, N. B., Nybo, L., Seneviratne, S. I., Vanos, J., & Jay, O. (2021). Hot weather and heat extremes: health risks. *The Lancet*, *398*(10301), 698–708. https://doi.org/10.1016/S0140-6736(21)01208-3Fan, X., Miao, C., Duan, Q., Shen, C., & Wu, Y. (2020). The Performance of CMIP6 Versus CMIP5 in Simulating Temperature Extremes Over the Global Land Surface. *Journal of Geophysical Research: Atmospheres*, *125*(18), 1–16. https://doi.org/10.1029/2020JD033031Guo, X., Huang, J., Luo, Y., Zhao, Z., & Xu, Y. (2017). Projection of heat waves over China for eight different global warming targets using 12 CMIP5 models. *Theoretical and Applied Climatology*, *128*(3–4), 507–522. https://doi.org/10.1007/s00704-015-1718-1Hong Kong Observatory (2020). *Number of Very Hot days*. Last modified January 30, 2020. Retrieved from https://www.hko.gov.hk/en/cis/statistic/vhotday_statistic.htmHong, S. Y., Dudhia, J., & Chen, S. H. (2004). A revised approach to ice microphysical processes for the bulk parameterization of clouds and precipitation. *Monthly Weather Review*, *132*(1), 103–120. https://doi.org/10.1175/1520-0493(2004)132<0103:ARATIM>2.0.CO;2Horton, R. M., Mankin, J. S., Lesk, C., Coffel, E., & Raymond, C. (2016). A Review of Recent Advances in Research on Extreme Heat Events. *Current Climate Change Reports*, *2*(4), 242–259. https://doi.org/10.1007/s40641-016-0042-xIntergovernmental Panel

on Climate Change. (2021). In Masson-Delmotte, V., P. Zhai, A. Pirani, S.L. Connors, C. Péan, S. Berger, N. Caud, Y. Chen, L. Goldfarb, M.I. Gomis, M. Huang, K. Leitzell, E. Lonnoy, J.B.R. Matthews, T.K. Maycock, T. Waterfield, O. Yelekçi, R. Yu, and B. Zhou (Eds.), Climate change 2021: The physical science basis. Contribution of Working Group I to the sixth assessment report of the Intergovern-mental Panel on Climate Change. Cambridge University Press. Kovats, R. S., & Hajat, S. (2008). Heat stress and public health: A critical review. *Annual Review of Public Health*, *29*, 41–55. https://doi.org/10.1146/annurev.publhealth.29.020907.090843Liu, K. (2020). A method to improve wind speed and temperature simulation results for the weather research and forecasting model by refining surface roughness length and background albedo, (Master thesis). Retrived from Hong Kong University of Science and Technology. (https://doi.org/10.14711/thesis-991012879966903412). Hong Kong, MI: Hong Kong University of Science and Technology. Perkins, S. E., & Alexander, L. V. (2013). On the measurement of heat waves. *Journal of Climate*, *26*(13), 4500–4517. https://doi.org/10.1175/JCLI-D-12-00383.1Perkins, S. E., Alexander, L. V., & Nairn, J. R. (2012). Increasing frequency, intensity and duration of observed global heatwaves and warm spells. *Geophysical Research Letters*, *39*(20), 1–5. https://doi.org/10.1029/2012GL053361Perkins, Sarah E. (2015). A review on the scientific understanding of heatwaves-Their measurement, driving mechanisms, and changes at the global scale. *Atmospheric Research*, *164–165*, 242–267. https://doi.org/10.1016/j.atmosres.2015.05.014Pleim, J. E. (2007). A combined local and nonlocal closure model for the atmospheric boundary layer. Part I: Model description and testing. *Journal of Applied Meteorology and Climatology*, *46*(9), 1383–1395. https://doi.org/10.1175/JAM2539.1Robine, J. M., Cheung, S. L. K., Le Roy, S., Van Oyen, H., Griffiths, C., Michel, J. P., & Herrmann, F. R. (2008). Death toll exceeded 70,000 in Europe during the summer of 2003. *Comptes Rendus - Biologies*, *331*(2), 171–178. https://doi.org/10.1016/j.crvi.2007.12.001Russo, S., Dosio, A., Graversen, R. G., Sillmann, J., Carrao, H., Dunbar, M. B., Singleton, A., Montagna, P., Barbola, P., & Vogt, J. V. (2014). Magnitude of extreme heat waves in present climate and their projection in a warming world. *Journal of Geophysical Research Atmospheres*, *119*(22), 12,500-12,512. https://doi.org/10.1002/2014JD022098S.Kain, J. (2004). *The Kain–Fritsch Convective Parameterization: An Update*. 170–181.Shi, Y., Ren, C., Cai, M., Lau, K. K. L., Lee, T. C., & Wong, W. K. (2019). Assessing spatial variability of extreme hot weather conditions in Hong Kong: A land use regression approach. *Environmental Research*, *171*(January), 403–415. https://doi.org/10.1016/j.envres.2019.01.041Thomas, N. P., Bosilovich, M. G., Marquardt Collow, A. B., Koster, R. D., Schubert, S. D., Dezfuli, A., & Mahanama, S. P. (2020). Mechanisms associated with daytime and nighttime heat waves over the contiguous United States. *Journal of Applied Meteorology and Climatology*, *59*(11), 1865–1882. https://doi.org/10.1175/JAMC-D-20-0053.1Wang, J., Chen, Y., Liao, W., He, G., Tett, S. F. B., Yan, Z., Zhai, P., Feng, J., Ma, W., Huang, C., & Hu, Y. (2021). Anthropogenic emissions and

urbanization increase risk of compound hot extremes in cities. *Nature Climate Change*, *11*(12), 1084–1089. https://doi.org/10.1038/s41558-021-01196-2Wang, P., Tang, J., Sun, X., Wang, S., Wu, J., Dong, X., & Fang, J. (2017). Heat Waves in China: Definitions, Leading Patterns, and Connections to Large-Scale Atmospheric Circulation and SSTs. *Journal of Geophysical Research: Atmospheres*, *122*(20), 10,679-10,699. https://doi.org/10.1002/2017JD027180Yang, X., Ruby Leung, L., Zhao, N., Zhao, C., Qian, Y., Hu, K., Liu, X., & Chen, B. (2017). Contribution of urbanization to the increase of extreme heat events in an urban agglomeration in east China. *Geophysical Research Letters*, *44*(13), 6940–6950. https://doi.org/10.1002/2017GL074084